Geophysical Journal International

Geophys. J. Int. (2011) **187,** 371–384 doi: 10.1111/j.1365-246X.2011.05148.x

Seismo-volcano source localization with triaxial broad-band seismic array

L. A. Inza,[1,2,4] J. I. Mars,[1] J. P. Métaxian,[2] G. S. O'Brien[3] and O. Macedo[4]

[1] *GIPSA-LAB/DIS/UMR* 5216 *Institut Polytechnique de Grenoble, France. E-mail: ainzac@gmail.com*
[2] *Institut des Sciences de la Terre IRD* R219 *CNRS, Université de Savoie, Campus Scientifique,* 73376 *Le Bourget du Lac Cedex, France*
[3] *School of Geological Sciences, University College Dublin, Belfield, Dublin* 4, *Ireland*
[4] *Instituto Geofisico del Peru, IGP, Peru*

Accepted 2011 July 10. Received 2011 July 6; in original form 2010 October 12

SUMMARY

Seismo-volcano source localization is essential to improve our understanding of eruptive dynamics and of magmatic systems. The lack of clear seismic wave phases prohibits the use of classical location methods. Seismic antennas composed of one-component (1C) seismometers provide a good estimate of the backazimuth of the wavefield. The depth estimation, on the other hand, is difficult or impossible to determine. As in classical seismology, the use of three-component (3C) seismometers is now common in volcano studies. To determine the source location parameters (backazimuth and depth), we extend the 1C seismic antenna approach to 3Cs. This paper discusses a high-resolution location method using a 3C array survey (3C-MUSIC algorithm) with data from two seismic antennas installed on an andesitic volcano in Peru (Ubinas volcano). One of the main scientific questions related to the eruptive process of Ubinas volcano is the relationship between the magmatic explosions and long-period (LP) swarms. After introducing the 3C array theory, we evaluate the robustness of the location method on a full wavefield 3-D synthetic data set generated using a digital elevation model of Ubinas volcano and an homogeneous velocity model. Results show that the backazimuth determined using the 3C array has a smaller error than a 1C array. Only the 3C method allows the recovery of the source depths. Finally, we applied the 3C approach to two seismic events recorded in 2009. Crossing the estimated backazimuth and incidence angles, we find sources located 1000 $\pm$ 660 m and 3000 $\pm$ 730 m below the bottom of the active crater for the explosion and the LP event, respectively. Therefore, extending 1C arrays to 3C arrays in volcano monitoring allows a more accurate determination of the source epicentre and now an estimate for the depth.

Key words: Time-series analysis; Fourier analysis; Spatial analysis; Volcano seismology; Explosive volcanism; Volcano monitoring.

1 INTRODUCTION

Source location (backazimuth and depth determination) is a fundamental goal in volcano monitoring. Long-period (LP) events and tremor, which can be theoretically related to fluid motion, constitute the main classes of seismic events observed on andesitic volcanoes (Chouet 1996). Locating these events is therefore necessary to better understand the eruptive dynamics and to improve the knowledge of the magmatic system. The lack of clear body-wave phase arrivals and emergent onsets in LP events and tremor makes locating these events extremely difficult using classical hypocentre determination methods based on phase picking and calculation of traveltimes. Other location methods have been used in recent years including a method based on the spatial distribution of seismic amplitudes to locate eruptive tremor sources on the Piton de la Fournaise volcano Battaglia & Aki (2003) and to track tremors produced by lahars on Cotopaxi volcano (Kumagai *et al.* 2009). De Barros *et al.* (2009) used a cross-correlation technique to locate LP events on Mt Etna using a dense seismic network, also. Full waveform inversion has been carried out to not only constrain the source mechanism but to locate the LP events (Ohminato *et al.* 1998; Chouet 2003; Chouet *et al.* 2005; Lokmer *et al.* 2007). More recently O'Brien *et al.* (2011) used a time-reverse method to locate two families of LP events on Mt Etna. Here we focus on the multicomponent array method for locating LP events. Dense one-component (1C) array methods based on time delays between close sensors, giving an estimation of the slowness vector of the wavefront propagating across the array, have been used by several authors and applied to a great variety of volcanoes. For example (Saccorotti & Del Pezzo 2000; La Rocca *et al.* 2004) applied dense 1C array techniques to locate

explosive activity at Stromboli. Almendros *et al.* (2002) characterized the spatial extent of a hydrothermal system at Kilauea volcano by using similar techniques. Métaxian *et al.* (2002) used several small dense arrays to locate LP events and tremor sources at Arenal volcano (Costa Rica) and Di Lieto *et al.* (2007) used two dense 1C arrays of short period seismometers to track volcanic tremor at Mt. Etna. Dense 1C array methods usually consist of only the vertical seismic component and allow a good estimation of the backazimuth of the wavefield. Unfortunately, the depth estimation is poorly resolved because the incidence angle is very difficult to determine. To overcome this problem, triaxial sensors (3C) can be used. In this work we focus on the improvement in backazimuth resolution and depth determination obtained by three-component (3C) rather than 1C seismometers. In our study two 3C arrays were installed on Ubinas volcano, Peru, in 2009 March to determine the backazimuth and depth of the seismo-volcano sources. The two small-aperture, cross-shaped seismic arrays consisted of 12 3C broad-band seismometers. One of the main scientific questions related to the eruptive process at Ubinas is the relationship between the magmatic explosions and the LP swarms preceding these events by several tens of minutes to a few hours (Macedo *et al.* 2009). Source location of the LP events with a higher resolution compared to the 1C dense array methods, particularly in the depth determination, is the main objective of this work. To achieve this goal, and before working with real wavefield data we performed several numerical simulations of seismic wave propagation using a 3-D digital elevation map and heterogeneous velocity model determined from a tomography study (Monteiller *et al.* 2005). Sources were placed at different depths below the crater, and receivers are situated at the same positions as the two experimental cross-shaped arrays. A high-resolution method based on the multiple signal classification (MUSIC technique) developed by Bienvenu & Kopp (1983) and Schmidt (1986), but adapted to the 3C case, is applied to the synthetic data to determine the backazimuth, the wavefield velocity and the incidence angle for both arrays and all sources. This procedure is then applied to the real data recorded in 2009 March.

2 UBINAS VOLCANO

Ubinas volcano (16 22′S, 70 54′W; altitude 5672 m) began to erupt on 2006 March 25 after nearly 40 years of quiescence. Situated in the Central Volcanic Zone (CVZ, southern Peru), Ubinas volcano is an active andesitic stratovolcano truncated in the upper part by a caldera 600 m in diameter (De Silva & Francis 1991). The caldera floor is a flat area lying approximately 5100 m above sea level. The active crater is situated in the southern section; the bottom is 300 m under the caldera floor (Fig. 1a). Ubinas is considered the most active Peruvian volcano during the last 500 years, threatening 3500 people living on the edge of the Ubinas valley (Rivera *et al.* 1998). Arequipa airport, situated 60 km east of the volcano, has been closed several times since 2006 due to ash emissions. The Instituto Geofisico del Peru (IGP) with the cooperation of the Institut de Recherche pour le Developement (IRD), under the 6th Framework Programme EU project VOLUME (http://www.volume-project.net/) started seismic monitoring of the volcano to understand the activity associated with this eruptive sequence. A network of four digital 1 Hz stations with a radio telemetry system has been operating since 2006. Data are transmitted to Arequipa observatory. At the time of the experiment, the eruption was characterized by almost permanent ash emissions. Two main types of degasification were observed: (1) exhalations rising a few hundred metres above the crater rim and (2) plumes produced by explosions that may reach 10 km, and are critical to aircraft safety. This activity is thought to be related to a magmatic plug positioned at the bottom of the southern part of the caldera wall (Macedo *et al.* 2009).

3 PROCESSING APPROACH

3C broad-band seismic array data are suitable for multidimensional signal processing techniques, where the size, shape, aperture of seismic antenna are designed to avoid spatial and temporal aliasing (Mars *et al.* 2004). We consider the scenario of an arbitrarily spaced array of triaxial sensors identically oriented and with identical instrument responses (Fig. 2). To explain the method, we suppose P sources travelling from different directions, and arriving at the antenna of N triaxial sensors ($P < N$). Eq. (1) $w_n(t)$ represents the signal recorded by one component of the the n-th sensor in the time–space domain.

$$w_n(t) = \sum_{p=1}^{P} s_p(t - \tau_{n,p}) + b_n(t); \quad n = 0, 1, \ldots, N-1, \tag{1}$$

where, $s_p(t)$ is the p-th source signal, $\tau_{n,p}$ is the relative propagation time delay of the p-th source for the n-th sensor and the $b_n(t)$ represents the noise of one component of the n-th sensor. The noise $b_n(t)$ is usually assumed to be uncorrelated with the sources and both temporally and spatially white with Gaussian variance σ_B^2. The corresponding relative propagation time delay is defined as $\tau_{n,p} = \mathbf{d_n} \cdot \mathbf{u}(\theta_p, \phi_p)$, where, $\mathbf{d}_n$ is the relative position vector of sensor 'n' with respect to the first sensor located at (0,0,0) and $\mathbf{u}(\theta_p, \phi_p)$ is the slowness vector indicating the direction of the p-th source. The slowness vector is given in the eq. (2), note that its module is the reciprocal of velocity v_o of the uppermost layer beneath the array.

$$\begin{aligned}\mathbf{u}_p &= \mathbf{u}(\theta_p, \phi_p) \\ &= \frac{1}{v_o}[-\cos(\theta_p)\sin(\phi_p) - \sin(\theta_p)\sin(\phi_p) - \cos(\phi_p)]^T.\end{aligned} \tag{2}$$

The wavenumber vector is related to the slowness vector and defined as $\mathbf{k}_p = \frac{1}{\lambda_w}\frac{\mathbf{u}}{|\mathbf{u}|} = \frac{f_o}{v_o}\frac{\mathbf{u}}{|\mathbf{u}|}$, where λ_w is the wavelength for the frequency f_o and velocity v_o of the wavefield. The frequency wavenumber (f–k) representation of eq. (1) becomes

$$W_n(f_o) = \sum_{p=1}^{P} S_p(f_o)\exp(-2\pi j(\mathbf{d}_n \cdot \mathbf{k}_p)) + B_n(f_o), \tag{3}$$

where, $j = \sqrt{-1}$ and $W_n(f_o)$, $S_p(f)$ and $B_n(f)$ are the Fourier transforms of $w_n(t)$, $s_p(t)$ and $b_n(t)$, respectively. The antenna output of the eq. (1) for narrow-band signals can be represented in matrix form as

$$\mathbf{W(f_o)} = \mathbf{A(f_o)S(f_o)} + \mathbf{B(f_o)} \tag{4}$$

where, the $N \times P$ matrix $\mathbf{A(f_o)}$ is the 'array response matrix' or 'steering matrix' (Miron *et al.* 2006) and is given in eqs (5). The P sources are represented by a $P \times 1$ matrix as $\mathbf{S(f_o)} = [S_1(f_o), \ldots, S_P(f_o)]^T$.

$$\begin{aligned}\mathbf{A(f_o)} &= [\mathrm{a}(\theta_1, \phi_1), \mathrm{a}(\theta_2, \phi_2), \ldots, \mathrm{a}(\theta_P, \phi_P)], \\ \mathrm{a}_p(\theta_p, \phi_p) &= \frac{1}{\sqrt{N}}[1, \exp(-2\pi j(\mathbf{d}_2 \cdot \mathbf{k}_p)), \quad \ldots\ldots, \\ &\qquad \exp(-2\pi j(\mathbf{d}_N \cdot \mathbf{k}_p))]^T.\end{aligned} \tag{5}$$

Usually, $\mathbf{A(f_o)}$ is a full rank matrix assuming that the array manifolds $\mathrm{a}_p(\theta_p, \phi_p)$ with different path directions are independent. Note that

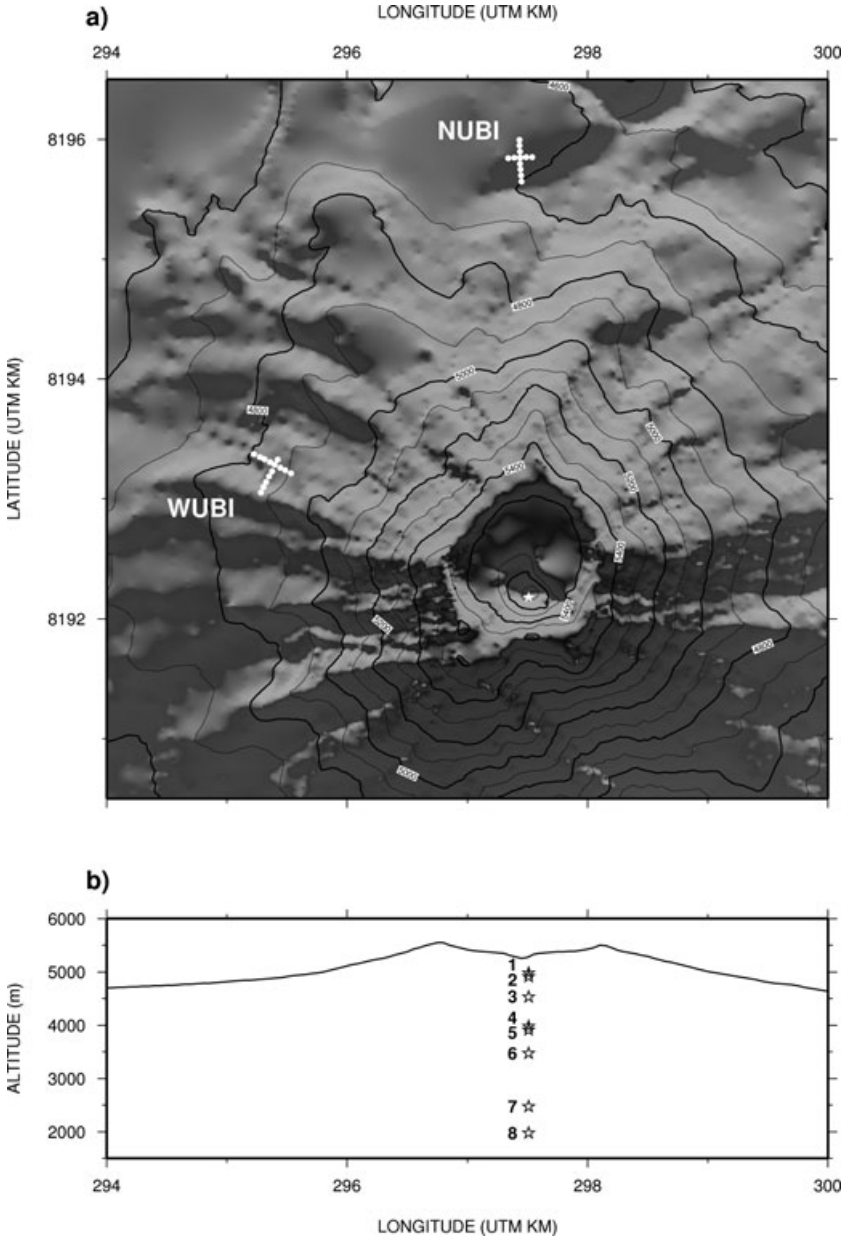

Figure 1. (a) Map of Ubinas volcano showing the location of the north (NUBI) and the northwest (WUBI) antennas, (b) East–West profile through the crater showing the position of the synthetic sources

the array manifold vector depends on the path direction of the signal through the wavenumber vector $\mathbf{k}_p$ for frequency f_o from the source p. The purpose of this paper is to develop and test a 3C-MUSIC algorithm to obtain a more robust estimation of the azimuth angle θ and a reliable incidence angle ϕ related to the source depth determination. This implies the sensors spatial position are known.

3.1 3C-MUSIC algorithm

MUltiple SIgnal Classification (MUSIC) is an eigenstructure subspace analysis method, that is widely used in geophysics, particularly to enhance the signal-to-noise ratio to estimate the direction of arrival of multiple waves impinging the array. The MUSIC uses the noise-subspace eigenvectors of the input cross-spectral matrix data and the steering matrix to form a null spectrum. The MUSIC method is applicable to an irregularly spaced array such as explained in Paulus & Mars (2010) and Wong & Zoltowski (2000). A data window for all components of N triaxial sensors array is selected, corresponding to the first arrival signal of either an explosion or LP event. A convenient way to find the dominant frequencies f_o is to integrate the power spectral density of each component. M frequency intervals around the bin f_o (energy peak) are sampled to estimate the cross-spectral matrix. The data model for every bin sampled is represented in the eq. (6) to consider the signal contribution of each component from triaxial sensor (around the frequency f0). Since we consider as realization each component, then the m-th sample ($m = 1, 2, \ldots, M$) can be represented as $N \times 3$ matrix data (N is the number of triaxial sensor).

$$\mathbf{W}_m = [Xn_m, \quad Yn_m, \quad Zn_m], \tag{6}$$

where, Xn, Yn and Zn represent the data vector of each component of the sensor for the sample m. Then the cross-spectral correlation

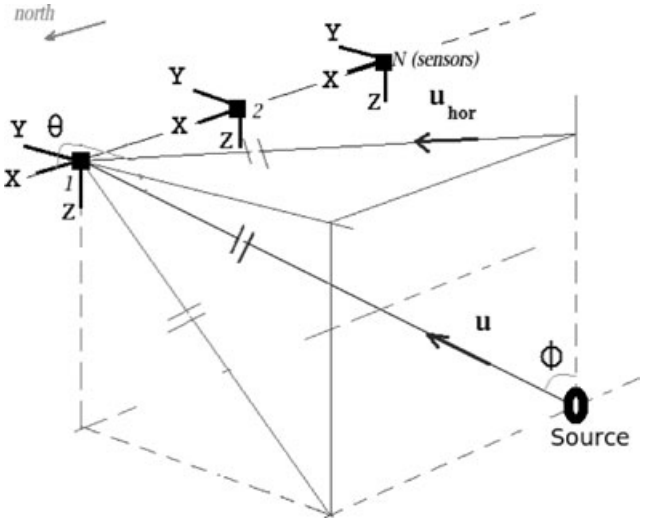

Figure 2. Model of triaxial sensors array for one source. *XYZ* represent north, east and vertical components, θ and ϕ are the azimuth and incidence angles.

estimates over M frequencies bins are defined in the eq. (7) (Paulus *et al.* 2005).

$$\widehat{\mathbf{\Gamma}}_W = \sum_{m=1}^{M} \xi\left\{\mathbf{W}_m\, \mathbf{W}_m^{\mathbf{H}}\right\}. \tag{7}$$

ξ denotes the mathematical expectation operator and $\mathbf{H}$ is the conjugate transpose. Following the assumption made for the eq. (8), the cross-correlation $\widehat{\mathbf{\Gamma}}_W$ can be written as (Paulus *et al.* 2005; Miron *et al.* 2005; Paulus & Mars 2010)

$$\widehat{\mathbf{\Gamma}}_W = \boldsymbol{A}\,\xi\{\mathbf{S}\,\mathbf{S}^H\}\,\boldsymbol{A}^H + \xi\{\mathbf{B}\,\mathbf{B}^H\},$$

$$\widehat{\mathbf{\Gamma}}_W(f_o) = \boldsymbol{A}\,(f_o)\,\widehat{\mathbf{\Gamma}}_s\,(f_o)\,\boldsymbol{A}^H\,(f_o) + \sigma_B^2\,(f_o)\,\mathbf{I}, \tag{8}$$

where, $\widehat{\mathbf{\Gamma}}_s\,(f_o) = \xi\{\mathbf{S}\,\mathbf{S}^H\}$ is the cross-spectral matrix of the source, $\mathbf{I}$ is the identity matrix and σ_B^2 is the variance of the noise. The eigenstructure of $N \times N$ cross-correlation matrix $\widehat{\mathbf{\Gamma}}_W$ solves the eigenvalues λ_n and eigenvectors $\mathbf{v_n}$ respectively (N = number of sensors), given by $\widehat{\mathbf{\Gamma}}_W = \sum_{n=1}^{N} \lambda_n \mathbf{v_n}\mathbf{v_n^H}$, with $\lambda_1 \geq \cdots \geq \lambda_P \geq \lambda_{P+1} > \cdots > \lambda_N \approx \sigma^2$. The P largest eigenvalues correspond to the signal subspace, while $N - P$ eigenvalues correspond to the noise subspace, usually no longer equal to σ_B^2. The 3C-MUSIC estimator is given in the eq. (9) by M_{3C} which computes the azimuth and incidence angles.

$$\mathbf{M}_{3C}\,(\theta, \phi) = \frac{1}{\mathbf{A}^H\,(\theta, \phi)\,\mathbf{\Pi}^{\perp}\mathbf{A}\,(\theta, \phi)}, \tag{9}$$

where, $\mathbf{\Pi}^{\perp} = \sum_{n=p+1}^{N} \mathbf{v}_n \mathbf{v}_n^H$ is the noise subspace projector. The following steps summarize the process of 3C-MUSIC method.

(i) Selection of the time window corresponding the first arrival for either an explosion or LP event.

(ii) Calculate the average power spectral density to determine the frequency bins f_0, we pointed out in eq. (6) considering M intervals around the frequency peak.

(iii) The cross-spectral matrix defined in eq. (7) can be estimated by eq. (10) (Miron *et al.* 2005; Paulus *et al.* 2005). Note that $\mathbf{W}_m$ is an $N \times 3$ matrix, eq. (6), therefore the $\widehat{\mathbf{\Gamma}}_x$ is an $N \times N$ Hermitian matrix.

$$\widehat{\mathbf{\Gamma}}_W = \frac{1}{M} \sum_{m=1}^{M} \left(\mathbf{W}_m \mathbf{W}_m^H\right). \tag{10}$$

(iv) Then perform the eigenstructure analysis of the cross-spectral matrix. The eigenvalues and eigenvectors are permuted from large to small. Then, one way to estimate the source number is looking for the largest eigenvalues, in our case a threshold is set up to 5 per cent the maximum for signal space. The remainder eigenvalues determine the noise subspace with which to build the noise projector.

(v) The 3C-MUSIC estimator is evaluated on a grid. The steering matrix (eq. 8) is computed on the grid, where the azimuth angle is between 0 and 2π, the incidence angle is between 0 and π and velocity would be set up between 10 and 5010 m s^{-1}.

(vi) First iteration: compute 3C-MUSIC estimator (eq. 9) by assuming the incidence angle $\phi = \pi/2$ (horizontal plane), whose the maximum value of the 3C-MUSIC spectrum will be the azimuth angle θ.

(vii) Second iteration: since the azimuth is estimate in the previous step, 3C-MUSIC estimator estimates the incidence angle ϕ (vertical plane) and velocity. So twice iterations more, using the incidence and azimuth values to refine the backazimuth, incidence and velocity.

4 DATA

A seismic experiment was carried out at Ubinas volcano between May and 2009 July. We deployed two cross-shaped antennas with triaxial broad-band seismometers as depicted in Fig. 1(a). NUBI antenna was installed on a flat area 4632 m above sea level. It consists of 12 Guralp CMG-6TD seismometers (see reference for Guralp manual). WUBI antenna was installed on a sloping area from 4752 m to 4883 m above sea level. It consists of six Guralp CMG-6TD and six GEOMAX seismometers (see reference for Geomax manual) both with 24 bit seismic recorders TITAN AGECODAGIS (dynamic range 120 dB) and high-accuracy GPS-based time synchronization. Continuous recordings were acquired with a sampling frequency of 100 Hz. The horizontal components of such seismometers were oriented to geographical coordinates west–east (Y component) and south–north (X component), respectively (Fig. 2). The distances between seismometers was set to approximately 50 m. Each seismometer location was surveyed by Trimble GPS (GeoXH, accuracy 0.3 m). 17 explosion earthquakes and 450 of LP events were recorded during the experiment. A full waveform synthetic data set was generated to test the accuracy of the location methods. The synthetic data set was created using a digital elevation map of Ubinas topography and the 2009 experimental array locations. A 3-D discrete numerical elastic lattice method O'Brien & Bean (2004) was used to propagate waves in the structure with eight broad-band isotropic sources (Fig. 1b) located beneath the summit. Altitudes of each source is indicated in Table 1. The velocity structure was generated from a tomography study (Monteiller unpublished)

Table 1. Distance between the calculated and real position of each synthetic source, mean quadratic radius and altitude of each source.

Source Number	Distance to the source (m)	R (m)	Altitude (m)
1	200	450	4972
2	140	500	4912
3	220	570	4532
4	330	630	3972
5	300	630	3912
6	120	750	3472
7	390	800	2472
8	500	820	1972

assuming a density of 2300 kg m^{-3}. Sample rate of the synthetic was 100 Hz.

4.1 Synthetic data analysis

To investigate the performance of the 3C-MUSIC technique, we applied it to our synthetic data set. For source number 3 (Fig. 1b) and synthetic array NUBI a 1 s time window including the first arrival was selected (Fig. 3 a). To find the dominant frequency, we averaged the power spectral density computed for the selected time window of each component and for each receiver. The dominant energy peak is located at 2.3 Hz (Fig. 3b). The cross-spectral matrix was then calculated by using 32 windows around the peak frequency. In the first stage, we determined the eigenvectors corresponding to the noise subspace, which gives the projector. In the second stage, we calculated the steering vector which consists of the slowness vector estimated between 0 and 2π with steps of 3.6°. Given the projector and the steering vector, we obtained the 3C-MUSIC spectrum represented in Fig. 4(a). The maximum amplitude of the spectrum gives the backazimuth and the velocity. The largest estimator point is located at 181 $\pm$ 3° for the backazimuth and 2900 $\pm$ 75 m s^{-1} for the velocity. The vertical and horizontal cross-section of the 3C-MUSIC spectrum are shown in Figs 4(b) and (c). The incidence angle is deduced from the backazimuth and velocity. We found 85.5 $\pm$ 6° as shown in Fig. 4(d). The errors are estimated by taking the peak width of 95 per cent of the maximum amplitude. These values agree well with the numerical model values. We applied the same analysis to the synthetic data generated for both arrays and for all eight sources. To compare the 3C and 1C methods, we also analysed the same synthetic data set using only the vertical components. The results are shown in the Figs 5(a) and (b) for NUBI and WUBI antennas, respectively. Backazimuth results obtained both with the 3C-MUSIC and the 1C-MUSIC fit well with the model values for both antennas. Errors are $\pm$3° and $\pm$6°, with the 3C and the 1C-MUSIC algorithm, respectively. However, the incidence angles are significantly different between the 3C-MUSIC and the 1C-MUSIC analysis.

For NUBI antenna, values vary from 55° for the deepest source to 93° for source 1. These incident angles are consistent with the variation of the source depths. Errors are $\pm$6° for the 3C-MUSIC analysis. These errors allow us to distinguish source depths separated by several hundreds of metres but are unable to separate close sources such as 1 and 2 or sources 4 and 5. The 1C-MUSIC analysis gives depths close to the model values for the superficial sources (1, 2 and 3) while depths for sources 4, 5, 6, 7 and 8 are far away from the model values. The incident angle remains approximately the same value, around 90°. The error obtained with the 1C-MUSIC processing is $\pm$12°. None of the sources can be distinguished with the 1C-MUSIC analysis.

For WUBI antenna, the 3C-MUSIC analysis gives incident angles between 43° for source 8 and 94° for source 1 (Fig. 5b). For WUBI, solutions follow the depth variation with errors of approximately 6°. The 1C-MUSIC analysis gives higher incident angles than the model values (90° for source 6 to 156° for source 1). Errors are larger than the 3C algorithm at approximately $\pm$15°. The 1C-MUSIC analysis does not give reliable solutions for any of the synthetic source depths. In this case, it seems that the solutions are affected by the topography below the antenna and possibly by the inclined free surface. Similar results are observed for the velocity. In summary, incident angles obtained by the 3C-MUSIC algorithm are close to

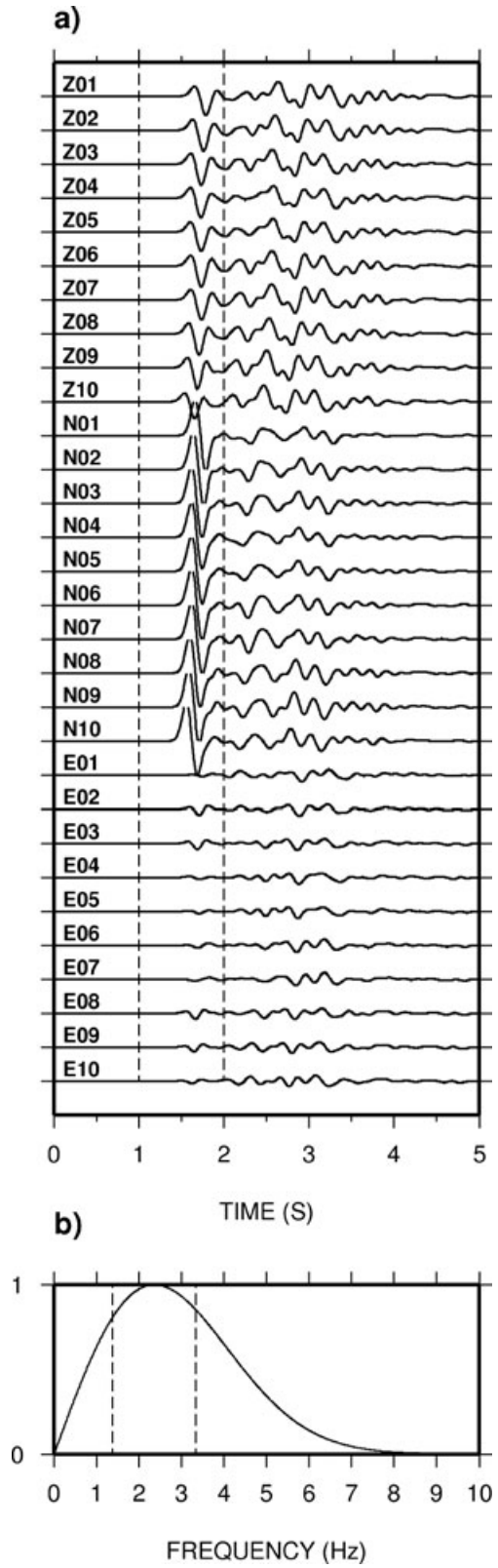

Figure 3. (a) The vertical (Z), north (N) and east (E) synthetic seismogram from NUBI antenna, (b) averaged energy spectrum calculated for all the receivers and all the components. The vertical dash lines in (a) indicate the time window selected for the processing. The vertical dash lines in (b) represent the frequency windows used for the cross-spectral matrix calculation.

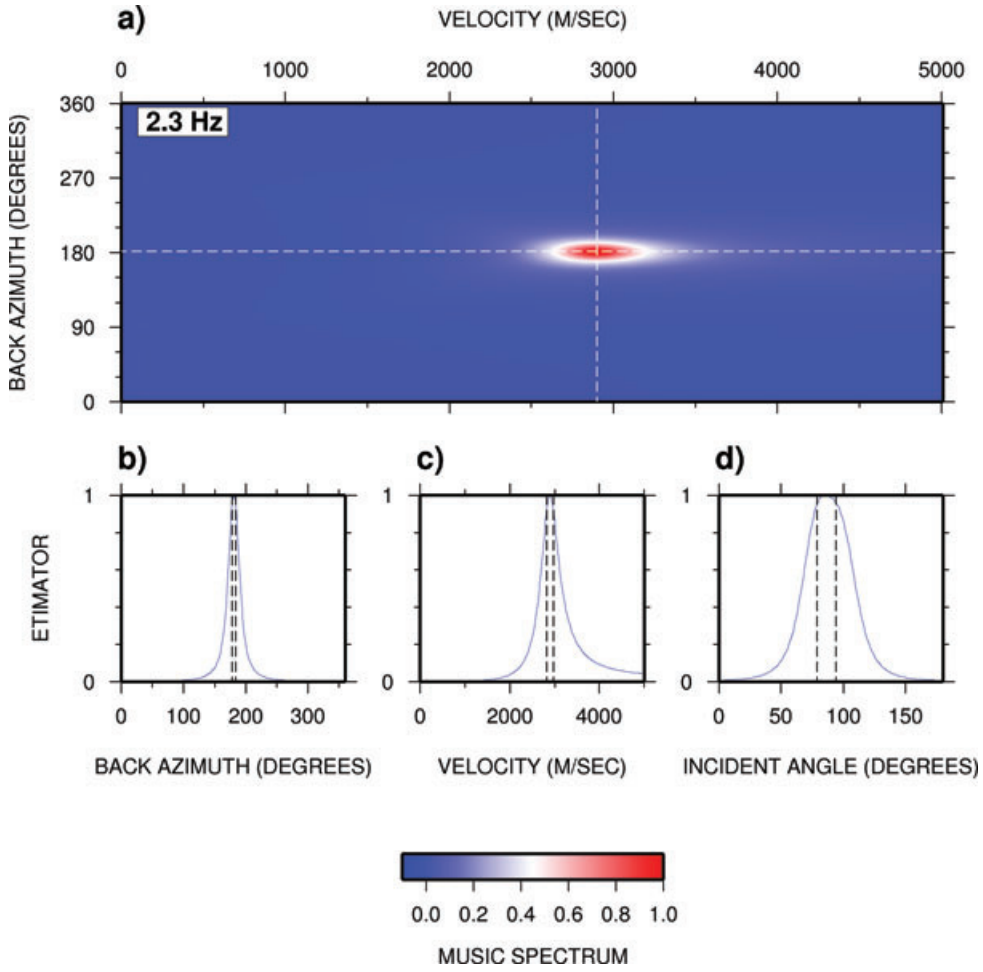

Figure 4. (a) Normalized 3C-MUSIC spectrum calculated with synthetic data generated at source 3 for NUBI antenna. The central frequency used for the cross-spectral matrix calculation (Fig. 3b) is indicated in the upper left of the spectrum. (b) Normalized backazimuth profile (cross-section at velocity 2900 m s^{-1}). (c) Normalized velocity profile (cross-section at backazimuth at 181°). (d) Normalized incidence angle. The vertical dotted lines represent the error 95 per cent range.

the theoretical values for both antennas, whereas those obtained with the 1C-MUSIC are not reliable.

In the following, we examine how crossing the source directions obtained with both antennas to delimit the source area. The backazimuth and the incident angle can be represented as Gaussian variables with mean θ ($0 \leq \theta \leq 360°$) and ϕ ($0 \leq \phi \leq 120°$) and standard deviations σ_θ and σ_ϕ corresponding to the values found in the analysis. This allows the definition of a probability density function (PDF) $\rho(\theta^k)$ of the backazimuth and a PDF $\rho(\phi^k)$ of the incident angle for each array k. $\rho_1(\theta^k)$ and $\rho_1(\phi^k)$ are shown in Fig. 6 as rose diagrams in the horizontal plane for the backazimuths and in the vertical planes oriented N–S and W–E for the incident angles.

The last step is to locate the source by using the information obtained at each antenna. For each point with geographical coordinates (x,y,z) in the source region and each array k, the backazimuths $\theta^k(x, y, z)$ and the corresponding value of $\rho_1(\theta^k)$, as well as the incident angle $\phi^k(x, y, z)$ and the corresponding value of $\rho_1(\phi^k)$ can be calculated. To represent the results the PDF of the source position is derived from the different PDFs of the backazimuth and the incident angle (Métaxian *et al.* 2002).

$$\rho_2(x, y, z) = \prod_{k=1}^{2} \rho_1(\theta^k(x, y, z)) \cdot \rho_1(\phi^k(x, y, z)). \quad (11)$$

The maximum likelihood of the PDF ρ_2 yields an estimate of the source location. We define the mean quadratic radius $R = \sqrt{(\sigma_1^2 + \sigma_2^2 + \sigma_3^2)/3}$, where σ_1^2, σ_2^2 and σ_3^2 are the principal variances of $\rho_2(x, y, z)$. We gathered in Table 1 the results obtained for the mean quadratic radius and the distance between the real position and the maximum likelihood of the PDF describing the source position. Both values have generally higher values for deeper sources, which would indicate a decrease of the resolution of the method for increasing depths. It is also notable that the mean quadratic radius that we consider as an estimate of the error is always much greater than the distance between the real and calculated source position. Hence, 3C-MUSIC allows to locate the synthetic sources, in all the cases. Moreover, it is interesting to note that our estimation of the error is probably overestimated in some cases. Fig. 6 shows in detail the results obtained for each synthetic source. The horizontal position is well determined for all sources. Looking at the vertical views, the PDF of the source position is well centred on synthetic sources for the two highest sources (Figs 6a and b). Uncertainty is larger for the source 3 positioned at the altitude of 4532 m (Fig. 6c). This source cannot be distinguished from sources 1 and 2 positioned at 4972 m and 4912 m, respectively. The PDF of the source position gives a good solution for sources 4 and 5 (Figs 6d and e). These sources can be clearly differentiated from sources 1, 2 and 3. It is more complicated to differentiate source 6 from source 5, which is

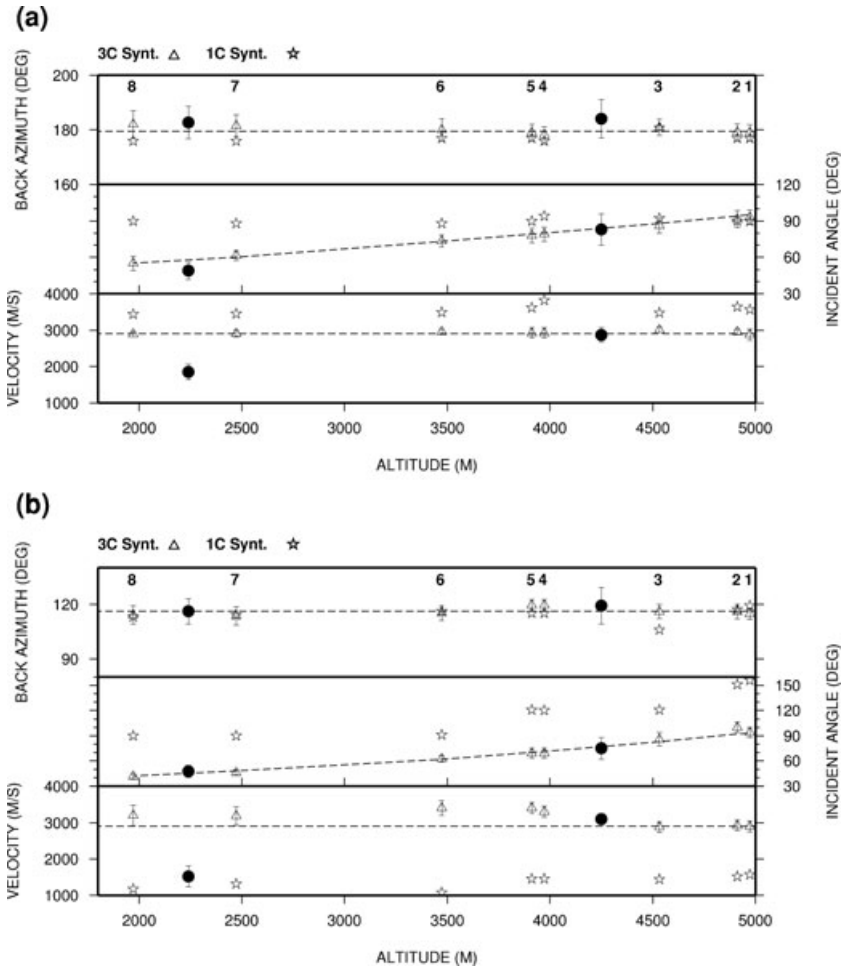

Figure 5. Results obtained for the synthetic data calculated for the eight sources. Open triangles and open stars represent results obtained with the 3C-MUSIC and 1C-MUSIC, respectively. Sources are numbered as in Fig. 1(b). (a) Backazimuth, incidence angle and apparent velocity for NUBI antenna. (b) Backazimuth, incidence angle and apparent velocity for WUBI antenna. Dashed lines represent the values. The filled circles represent the real data results.

located 430 m above (Figs 6f). In the same manner, it is not clearly possible to differentiate sources 7 and 8 (Figs 6g and h). On the other hand, 3C-MUSIC allows to easily differentiate the two groups of sources 5, 6 and 7, 8.

The PDF results corresponding to source 6 is situated near the the source 5, which also prevents us in this case from distinguishing sources 5 and 6. The PDF of source position would be better determined with more antennas. Nevertheless, shallow and deep sources are clearly distinguished as shown in the Figs 6(f)–(h).

4.2 Real data analysis

In this section, we discuss the performance of 3C-MUSIC method by applying it to two examples of real seismic events recorded at Ubinas volcano. We consider an explosion earthquake signal and an LP event. These two kinds of events are representative of the seismic activity that recorded during the experiment. The selected events, recorded, respectively, at 00:37 for the LP event and at 01:27, 2009 June 2 for the explosion are shown in Fig. 7. The data were corrected for the instrument response and bandpass filtered between 1 and 10 Hz. Fig. 8 shows the antenna (NUBI) energy spectrum average obtained from 2 s of signal including the first arrival. The dominant peak is centred at 3.9 Hz for the LP event. The maximum of the 3C-MUSIC spectrum gives a backazimuth of 183 $\pm$ 6°, a velocity of 1851 $\pm$ 221 m s^{-1} and an incidence angle of 49 $\pm$ 7°. For WUBI, we obtained a backazimuth of 116 $\pm$ 7°, a velocity of 1520 $\pm$ 295 m s^{-1} and an incidence angle of 47 $\pm$ 7°. The dominant peak is centred at 2.4 Hz for the explosion. We find a backazimuth of 184 $\pm$ 5°, a velocity of 2975 $\pm$ 125 m s^{-1} and an incidence angle of 86 $\pm$ 7°. For WUBI, we obtained a backazimuth of 119 $\pm$ 6°, a velocity of 3100 $\pm$ 120 m s^{-1} and an incidence angle of 75 $\pm$ 7°. We used eq. (11) to calculate the PDF of the source position for the LP event and the explosion earthquake. Results are shown in Fig. 9. The maximum likelihood of the PDF is situated 3000 m below the bottom of the crater at the altitude of 2240 m. The radius R is 730 m. The source area of the explosion is situated 150 m West and 1000 m below the bottom of the crater at an altitude of 4200 m, the radius R is 660 m.

5 DISCUSSION

5.1 Capabilities of the method

3C-MUSIC gives good results for locating seismo-volcanic sources. Results obtained with synthetic sources generated in an homogeneous medium are convincing. The main contribution of 3C-MUSIC compared with 1C-MUSIC is the determination of the depth. Only the 3C seismic array can receive the entire wavefield in three

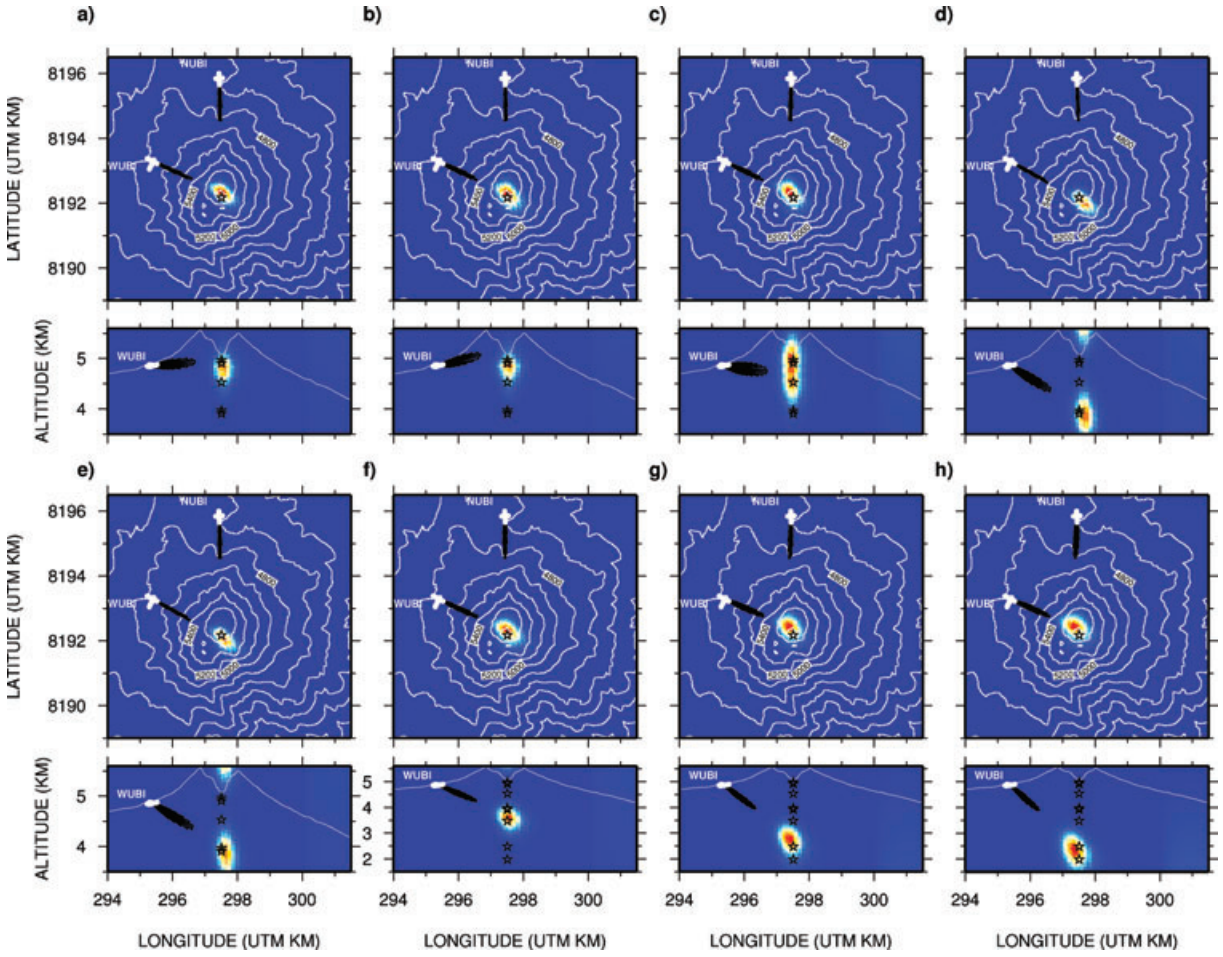

Figure 6. Probability density function of the source position ρ_2 for the eight synthetic sources. Horizontal view represented at the source depth and vertical view oriented west–east crossing the maximum likelihood of ρ_2 for the sources at the depths of (a) 4972 m, (b) 4912 m, (c) 4532 m, (d) 3972 m, (e) 3912 m, (f) 3472 m, (g) 2472 and (h) 1972, respectively. The PDF $\rho_1(\theta^k)$ and $\rho_1(\phi^k)$ are represented as rose diagrams with an increase of 5°. White points represent the sensor positions. A different vertical scale is used for a, b, c, d and e (altitude between 3.5 and 5.6 km) and f, g and h (altitude between 1.5 and 5.6 km).

dimensions, where the full energy impinging the antenna can be well determined. The depth resolution is related to the incidence angles estimation. The incidence angle is affected by the intersensor level differences, in our case, the antennas have a good distribution on horizontal plane, it is the reason that azimuth angle can be well determined with 3C-MUSIC and 1C-MUSIC too. On the vertical plane the intersensor level differences is not as well as the horizontal case, then the signal-to-noise ratio of the signal in this analysis plays an important role to increase the resolution of the estimator. Especially our analysis is on the first arrival part of the signal, where the signal-to-noise ratio is still weak. Then 1C array data is not enough to get a good resolution on the MUSIC estimator, it has presented a broad lobe in the spectrum. We observed the average signal-to noise ratio for the first arrival section of LP event recorded on NUBI antenna is 6 dB bigger the vertical components only. The incident angle is determined with a weaker resolution than the backazimuth. This can be explained by the spatial distribution of the sensors constituting the antennas. Theoretically, the incident angle cannot be determined if all the sensors of the antenna are positioned in the same plane. Métaxian *et al.* (2009) defined an index of coplanarity ranging between 0 and 1 allowing to determine if the incident angle can be estimated or not for a given antenna geometry. The index of coplanarity is 0.08 for NUBI and 0.4 for WUBI. NUBI was set up on a plain of ash, whereas WUBI was installed on a steep and irregular slope (Fig. 1a). Thus, the antenna geometry seems to be a reasonable explanation of the lowest resolution obtained for the incident angle. Antenna geometries with index of coplanarity closest to 1 would probably have improved the incidence angle resolution.

An interesting subject, but not easy to deal with is the comparison of the resolution of the various methods for locating LP seismicity. It is a complicated task, which exceeds the framework of this paper. Several distinct methods have been applied in the last decade. Different approaches are used, such as attenuation of seismic amplitudes (Battaglia & Aki 2003), full waveform inversion (Chouet 2003; Chouet *et al.* 2005; Lokmer *et al.* 2007; Bean *et al.* 2008; De Barros *et al.* 2011), the semblance method (Kawakatsu *et al.* 2000; Almendros & Chouet 2003), cross-correlation methods (De Barros *et al.* 2009), time-reverse method (O'Brien *et al.* 2011) or array technics by slowness analysis (Saccorotti & Del Pezzo 2000; Almendros *et al.* 2001a, b; Métaxian *et al.* 2002; La Rocca *et al.* 2004; Garcia Yeguas *et al.* 2011). Moreover, these different techniques are adapted to different kinds of seismic arrays with different geometries and number of sensors. They are applied to volcanoes characterized by distinct dynamics and structures. One distinguishes two main families of techniques used for locating LP sources, techniques using (1) arrays constituted of plain sensor stations, which are generally spatially distributed around the volcano; (2) arrays formed of seismic antennas distributed generally on a

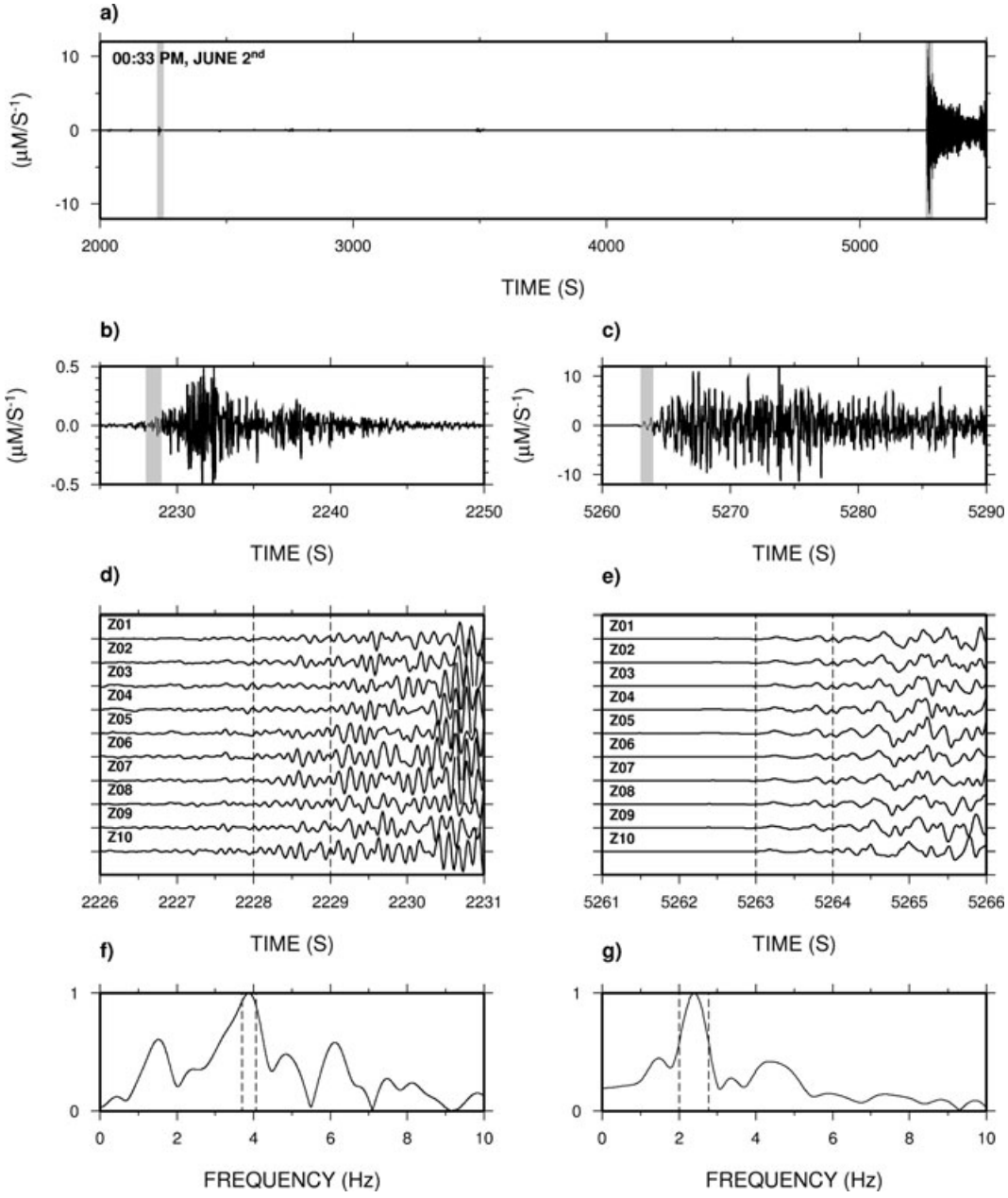

Figure 7. (a) *Z* component seismogram of the LP event and explosion earthquake recorded by the central station of NUBI antenna. The time and date of the first sample is indicated in the upper left of the record. Shaded zones represent part of the signals enlarged in (b) and (c). (d) and (e) *Z* component of the LP event and the explosion earthquake recorded by 10 stations of NUBI antenna. Waveforms correspond to the shaded parts of the signal in (b) and (c), filtered between 1 and 10 Hz. The vertical dashed lines in (d) and (e) indicate the time window selected for the processing. (f) and (g) Averaged energy spectrum calculated for all the receivers and all the components, where the vertical dashed lines represent the frequency windows used for the cross-spectral matrix calculation.

few sites (maximum 3 or 4), because of the high number of sensors needed for each antenna. In most of the location methods used with the arrays of the first category, the discrepancy between the model and the observations are quantified. It is the case for example for the attenuation of seismic amplitudes or for full waveform inversion methods. A grid search is performed to determine the best solution for a point source and to define an error region. The size of this region characterizes the resolution of the method. For antennas techniques, parameters characterizing the wave propagation through the array (azimuth apparent, slowness and incident angle) are estimated. These parameters are estimated on the basis of delay calculations between all the couples of sensors composing the antennas. The errors associated to delay calculation are quantified and included directly in the slowness vector estimation. One of the main limitation of array techniques is the plane wave assumption. Saccorotti & Del Pezzo (2000) pointed out several causes inducing errors in the time delays calculations and therefore in the resolution of location with antennas methods. These causes can be local velocity heterogeneities beneath the array, near-field effects (intertwining of *P* and *S* waves), near-sites scatterers, random velocity fluctuations, multipathing and interference phenomena. Neuberg & Pointer (2000) show that the plane wave approximation remains

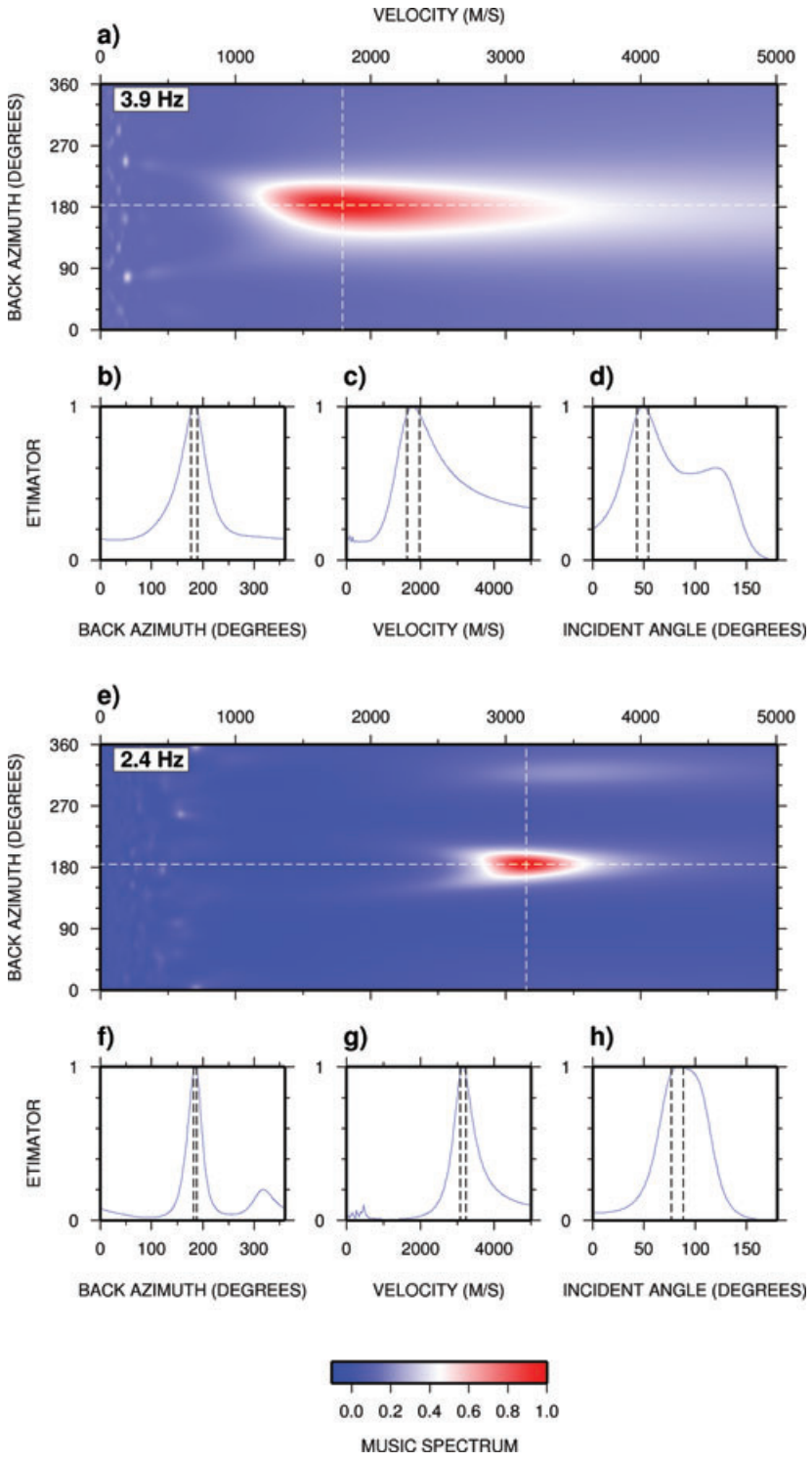

Figure 8. (a) Normalized 3C-MUSIC spectrum calculated with the LP event for NUBI antenna. The central frequency used for the cross-spectral matrix calculation (Fig. 7f) is indicated in the upper left of the spectrum. (b) Normalized backazimuth profile (cross-section at velocity 1794 m s^{-1}). (c) Normalized velocity profile (cross-section at backazimuth at 183°). (d) Normalized incidence angle. The vertical dotted lines represent the error range. (e) Normalized 3C-MUSIC spectrum calculated with the explosion earthquake for NUBI antenna. The central frequency used for the cross-spectral matrix calculation (Fig. 7g) is indicated in the upper left of the spectrum. (f) Normalized backazimuth profile (cross-section at velocity 3151 m s^{-1}). (g) Normalized velocity profile (cross-section at backazimuth at 184.5°). (h) Normalized incidence angle. The vertical dotted lines represent the error range.

valid if the dominant wavelength does not exceed twice the source depth, which is the case for the LP events and the explosions of Ubinas. Almendros *et al.* (2001a) applied the 1C-MUSIC technique to data recorded at Kilauea volcano with three seismic antennas. To estimate the error in the determination of the slowness vector, they took the region within which the slowness power spectrum is larger than 90 per cent of the maximum value. They estimated individual LP event locations to have an error of 200 m. This result is

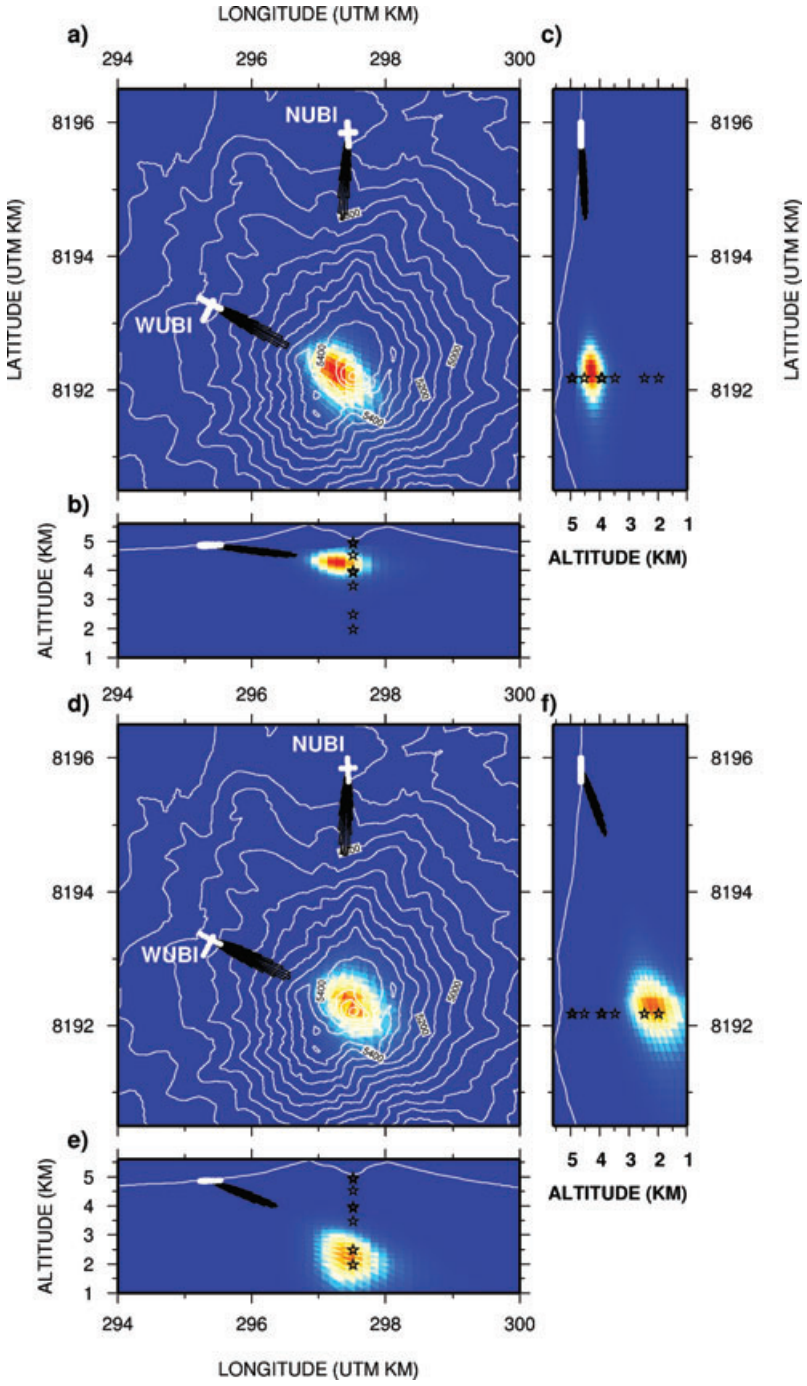

Figure 9. Probability density function of the source position ρ_2, for the explosion earthquake (a–c) and the LP event (d–f). (a) Horizontal view at 4200 m depth, (b) vertical view oriented west–east crossing the maximum likelihood of ρ_2, (c) same as (b) oriented north–south. (d) Horizontal view at 2240 m depth, (e) vertical view oriented west–east crossing the maximum likelihood of ρ_2, (f) same as (e) oriented north–south. The PDF $\rho_1(\theta^k)$ and $\rho_1(\phi^k)$ are represented as rose diagrams with an increment of 5°.

obtained by comparing slownesses derived from the data analysis with a slowness vector model calculated while taking into account the 3-D velocity model of Kilauea and the topography. This process of source location cannot be applied at Ubinas as the velocity model is not known. Hence, we stayed at the stage of crossing in the volcano volume the directions given by the backazimuth and the incident angle obtained at each antenna. This assumes a rectilinear propagation in a homogeneous medium between the source and the sensors, which is of course a strong approximation. All the location methods are highly dependent of the knowledge of the structure as well as the topography. Velocity structures are not yet known for most of the volcanoes. Even when a 3-D velocity model exists, the resolution of the model, particularly in the near surface (Bean *et al.* 2008), stems a strong limitation for locating LP events. Neuberg & Pointer (2000) pointed out the importance of topography on waveforms. They show that for broad-band waveforms, the angle of incidence as well as the backazimuth is affected by an inclined free surface. Tests performed with synthetics revealed that

the inclined free surface seems to influence strongly the 1C-MUSIC analysis at WUBI, but not the 3C-MUSIC analysis. Other causes of errors have been put in evidence, as the influence of the near-field effects. Lokmer *et al.* (2010) showed that the near-field term can introduce errors to the amplitude decay location technique, since the near-field term has variable decaying properties for small distances. On the other hand, this effect is not strongly pronounced for sources with a strong isotropic component and does not affect source locations when using full wave techniques as the near field is inherent in the simulations.

Finally, we used only two antennas for logistic reasons. Métaxian *et al.* (2002, 2009) studied the influence of the number of antennas and their spatial distribution on source location at Arenal volcano. We made similar tests at Ubinas by generating synthetics for two additional antennas situated East and South of the volcano. Results, show that the error is significantly smaller when using three or four antennas. However, at the same time, the deepest sources are found close, but beside the real positions when using four antennas, which clearly indicate the limitation induced by using a homogeneous medium. However, even with this approximation, tests made with two antennas and synthetics generated at eight different depths show that sources separated by depth of several hundreds of metres are easily differentiated by applying 3C-MUSIC. Consequently, it is reasonable to think that the explosion earthquake we analysed is not located superficially, but deep in the conduit. In the same manner, we conclude that the LP event is located deeper than the explosion.

5.2 Volcanological aspect

In the following, we discuss some of the possible mechanisms that might explain deep sources in the conduit for an explosion earthquake or an LP event. Fragmentation of viscous magma by brittle failure is thought to be responsible of explosions in silicic volcanoes (Alidibirov & Dingwell 2000). Melnik & Sparks (2002) have modelled unsteady conduit flow in explosive eruptions after unloading through dome collapse. These models have been applied to the episodes of explosive activity occurred shortly after dome collapse at Soufrière Hills volcano. The unloading triggers gas exsolution and magma rising in the conduit, increasing its internal pressure. An explosion is triggered when the internal pressure equals the tensile strength of the magma. Overpressure is responsible for the magma fragmentation generating gas-particle dispersion, which propagates to the exit of the conduit to form a volcanic column in the atmosphere (Melnik & Sparks 2002). Other studies also suggest that fragmentation occurs when a critical overpressure or critical elongation strain rate of magma is reached (Alidibirov & Dingwell 1996; 2000; Papale 1999).

Studying tuffisites veins in the dissected vent of rhyolite conduits at Torfakökull, Iceland, Tuffen *et al.* (2003) and Tuffen & Dingwell (2005) interpreted fault textures as resulting from shallow seismogenic faulting within rising magma during the emplacement of highly viscous lava flows. They suggest that the faulting process recorded in these conduits is consistent with many characteristics of LP and hybrid events during lava dome eruptions. Neuberg *et al.* (2006) proposed a seismic trigger model to explain source mechanism of LP events on Soufrière Hills, which are characterized by non-destructive, repetitive and stationary source location. This model is based on brittle failure of magma, the source location is proposed to mark the transition from ductile conduit flow to friction controlled magma ascent, approximately 1500 ± 100 m below the active dome. Given the above work proposed for modelling explosions and LP events at Soufrière Hills volcano, identical source models are envisaged for Ubinas. Indeed, as for Soufrière Hills, Ubinas explosions are characterized by short duration events (tens of seconds to one minute), fountain collapse consistent with abrupt halt of fragmentation, followed by slower degassing and patterns of repetitive explosions. Moreover, Vulcanian activity at Ubinas is also characterized by pulsations of explosions, with time intervals of a few hours to tens of hours between each event. During the two months of experiment, 17 vulcanian explosions were observed between the May 15 and the 2009 June 14, among which six occurred on May 25. No dome was observed at Ubinas, but a magmatic plug positioned at the bottom of the active vent (Macedo *et al.* 2009). Visual observations of ash pulses rising from hundreds of metres to several kilometres correlate with seismically recorded explosions. Slow degassing accompanied with pulses of ash emissions was almost continuous at Ubinas during the experiment. These pulses can be interpreted as releases of pressure resulting from fracturing or a sufficient permeability of the superficial solid cap of the plug. Such a process indicates pressure increases in the magma conduit probably induced by bubble growth. The occurrence of some LP events was also correlated visually with pulses of ash. The pulses cannot all be associated to an LP event. Variability in the intensity of the pulses could be observed and their number is much higher compared to the number of detectable LP. Ash emission associated with explosions and LP events could be clearly differentiated by the altitude reached by the column, but also by the intensity and the velocity of the ejection of ashes in the atmosphere. Unfortunately, particle velocities could not be measured and this assumption is based only on visual observations. According to Neuberg *et al.* (2006), the LP event can be interpreted as resulting from shear-fracturing of magma at the conduit walls. The fracturation level, which is considered by Neuberg *et al.* (2006) as the ductile to brittle transition zone where cracks open, is considered to correspond to the source position of the LP event in the conduit. We found the source located at 2240 ± 730 m a.s.l., which is approximately 3000 m below the bottom of the crater. The explosion, which occurs 50 min after the LP event is located at 4200 ± 660 m a.s.l, thus 2000 m above the LP source. There is no necessary relation between the two events. A lot of LP events occur without being followed by an explosion earthquake in the next hours or days. On the other hand, Traversa *et al.* (2011) who studied the time evolution of the LP seismicity rate prior to 143 explosion earthquakes recorded over a two-year period (2006–2008) at Ubinas, observed an acceleration of the LP rate above the background level during 2–3 h preceding the explosion onset. These results do not allow to establish any direct relation between the two events we are studying, but show that, in average, LP activity increases statistically before explosions, which implies necessarily an increase of gas ascent in the conduit. If the solidified cap keeps a sufficient level of permeability, the gas can escape through the fractures formed at the conduit walls. Hence, the internal pressure stays below the tensile strength of the magma. No explosion occurs in this case. Should the opposite occur, the gas accumulates in the conduit and the overpressure can generate fragmentation. The gas escaped following the fracturing of solidified magma at the conduit walls that produced the LP event may have been responsible for an increase of the internal pressure in the conduit and an overpressure state that may have initiated fragmentation.

Considering the mechanism of explosion and the onset of fragmentation, Traversa *et al.* (2011) found that the rate of LP events preceding another LP event shows similar pattern to the rate of LP events preceding explosions. The slope of the LP rate acceleration is smaller prior to an LP event and appears to be related to the energy

of the explosions, stronger for higher energy explosions (Traversa *et al.* 2011). This is a strong argument for a common mechanism for the generation of LP events and explosions at Ubinas. Analysis of the whole catalogue of data recorded during the experiment, including 17 explosions and 450 LP events has to be achieved to study more in detail the relation between LP events and explosions. Depth values found for the LP event and the explosion earthquake are consistent with results found on other silicic volcanoes. Druitt *et al.* (2002) estimated the drawdown depths of Vulcanian explosions at a few hundred metres to 2 km for Soufrière Hills volcano. On this same volcano, applying a classical method of arrival times to families of multiplets of LP events, Neuberg *et al.* (2006) located sources approximately 1500 ± 100 m below the active dome. Chouet *et al.* (2005) located sources of VLP signals generated by explosions at Popocatepetl from waveform inversion, 1500 m below the western crater wall. Using a similar inversion technique, Kumagai *et al.* (2011) located an explosion event at Tungurahua volcano 6 km below the crater. Analysing deposits at Katmai Volcano, Alaska, Hildreth (1987) found evidences that fragmentation occurred at depths of less than 1.5 km. More data have to be processed to confirm or to invalidate these results and to try to find a model that could explain the occurrence of LP events and explosions at different levels into the conduit. The determination of depth of LP events and explosion earthquakes should make it possible to carry constraints to the determination of eruptive dynamics.

6 CONCLUSIONS

We have presented a source localization method, 3C-MUSIC, based on the use of 3C arrays and, compared, with the 1C-MUSIC used in previous studies on volcanoes (Almendros *et al.* 2001a; Saccorotti *et al.* 2004). Synthetics have been generated for eight sources with elevations from 1972 m to 4950 m a.s.l. The backazimuths from the 3C-MUSIC correspond to the model values for both antennas with a resolution of $\pm 3^\circ$. 1C-MUSIC gives equivalent results, but with higher errors ($\pm 6^\circ$). The incident angle varies with depth when it is determined with the 3C-MUSIC. The incident angle is determined with an error of $\pm 6^\circ$ for NUBI and for WUBI. Knowing the distance from the centre of the antennas and the hypocentre of the sources, depth resolution can be deduced for each antenna. It is 500 m for NUBI and 400 m for WUBI. On the other hand, the 1C-MUSIC analysis does not allow the depth to be determined. It seems that the topography may affect the results obtained with the 1C-MUSIC and to a lesser extent the 3C-MUSIC. The velocity follows the same behaviour as the incident angle. The theoretical velocity has an accuracy of ± 150 m s^{-1} using the 3C-MUSIC algorithm. The 1C-MUSIC measures higher velocities at NUBI and lower velocities at WUBI. Finally, we located an LP event and an explosion earthquake recorded during the field experiment using the 3C-MUSIC. These signals are characteristic of the explosive activity observed at Ubinas volcano (Macedo *et al.* 2009). We found sources located at 2240 ± 730 m a.s.l. for the LP event and at 4200 ± 660 m a.s.l for the explosion. Consequently, the LP and the explosion source are situated 3000 m and 1000 m below the summit of the intrusive conduit, respectively. We conclude that 3C-MUSIC provides realistic estimates of the depth of volcanic sources, unlike the 1C-MUSIC or other antenna methods based on time delays measurements. The explosion earthquake and the LP event are interpreted as resulting, respectively, from a fragmentation process and shear-fracturing of the magma at the conduit walls. Given the performance of the 3C-MUSIC algorithm, we will apply it to other explosions and LP events recorded at Ubinas during the experiment to better characterize the eruptive dynamics of this volcano. In addition, the 3C-MUSIC will be tested with the IGP monitoring system to try to locate the seismic activity in real time. This algorithm is not restricted to volcanic sources but can be used to locate other types of non-volcanic signals.

ACKNOWLEDGMENTS

Adolfo Inza was partly funded by an IRD grant and the EU VOLUME project. Financial assistance for fieldwork from IRD, Université de Savoie and the EU VOLUME project are acknowledged. The experiment was performed with equipments from the Lithoscope French mobile network, the Université de Savoie and the University College Dublin. The relevant comments made by an anonymous reviewer and by Arthur Jolly greatly contributed to improve the manuscript. This work was funded by the 6th Framework EU Project no. 018471 VOLUME.

REFERENCES

Alidibirov, M. & Dingwell, D., 1996. Magma fragmentation by rapid decompression, *Nature*, **380,** 146–148.

Alidibirov, M. & Dingwell, D., 2000. Three fragmentation mechanisms for highly viscous magma under rapid decompression, *J. Volc. Geotherm. Res.*, **100,** 413–421.

Almendros, J. & Chouet, B., 2003. Performance of the radial semblance method for the location of very long volcanic signals, *Bull. seism. Soc. Am.*, **93,** 1890–1903.

Almendros, J., Chouet, B. & Dawson, P., 2001a. Spatial extent of a hydrothermal system at Kilauea volcano Hawaii, determined from array analysis of shallow long-period sismicity. Part I: method, *J. geophys. Res.*, **106,** 13 565–13 580.

Almendros, J., Chouet, B. & Dawson, P., 2001b. Spatial extent of a hydrothermal system at Kilauea volcano Hawaii, determined from array analysis of shallow long-period sismicity. Part II: results, *J. geophys. Res.*, **106,** 13 581–13 597.

Almendros, J., Chouet, B., Dawson, P. & Huber, C., 2002. Mapping the sources of the seismic wave field at Kilauea volcano, Hawaii, using data recorded on multiple seismic antennas, *Bull. seism. Soc. Am.*, **92,** 2333–2351.

Battaglia, J. & Aki, K., 2003. Location of seismic events and eruptive fissures on the Piton de la Fournaise volcano using seismic amplitudes, *J. geophys. Res.*, **108,** 2364, doi:10.1029/2002JB002193.

Bean, C.J., Lokmer, I. & O'Brien, G.S., 2008. Influence of near-surface volcanic structure on long-period seismic and moment tensor inversions simulated examples from Mount Etna, *J. geophys. Res.*, **113,** B08308, doi:10.1029/2007JB005463.

Bienvenu, G. & Kopp, L., 1983. Optimality of high resolution array processing using eigensystem approach, *IEEE-ASSP*, **33,** 1235–1247.

Chouet, B., 1996. Long-period volcano seismicity: its source and use in eruption forecasting, *Nature*, **380,** 309–316.

Chouet, B., 2003. Volcano seismology, *Pure appl. Geophys*, **160,** 739–788.

Chouet, B., Dawson, P. & Arciniega-Ceballos, A., 2005. Source mechanism of vulcanian degassing at Popocatepetl volcano, Mexico, determined from waveform inversion of very long period signals, *J. geophys. Res.*, **110,** B07301, doi:10.1029/2004JB005468.

De Barros, L., Bean, C.J., Lokmer, I., Saccoroti, G., Zuccarello, L., O'Brien, G.S. & Métaxian, J.-P., 2009. Source geometry from exceptionally high resolution long period event observations at Mt Etna during the 2008 eruption, *Geophys. Res. Lett.*, **36,** L24305, doi:10.1029/2009GL041273.

De Barros, L., Lokmer, I., Bean, C., O'Brien, G., Saccorotti, G., Métaxian, J., Zuccarello, L. & Patane, D., 2011. Source mechanism of long period events recorded by a high density seismic network during the 2008 eruption on Mt Etna, *J. geophys. Res.*, **116,** B01304, doi:10.1029/2010JB007629.

De Silva, S.L. & Francis, P.W., 1991. Volcanoes of the central Andes, *Geol. Mag.,* **129,** 253–254.

Di Lieto, B., Saccorotti, G., Zuccarello, L., La Rocca, M. & Scarpa, R., 2007. Continuous tracking of volcanic tremor at Mt Etna, Italy, *Geophys. J. Int.*, **169,** 699–705.

Druitt, T. *et al.*, 2002. Episodes of cyclic vulcanian explosive activity with fountain collapse at Soufriere Hills volcano, Montserrat, *Mem. Geol. Soc. London*, **21,** 281–306.

Garcia, Y.A., Almendros, J., Abella, R. & Ibanez, J., 2011. Quantitative analysis of seismic wave propagation anomalies in azimuth and apparent slowness at Deception Island volcano (Antarctica) using seismic arrays, *Geophys. J. Int.*, **184,** 801–815.

Hildreth, W., 1987. New perspectives on the eruption of 1912 in the Valley of Ten Thousand Smokes, Katmai National Park, Alaska, *Bull. Volcanol.*, **49,** 680–693.

Kawakatsu, H. et al., 2000. Aso-94: Aso seismic observation with broadband instruments, *J. Volc. Geotherm. Res.*, **101,** 129–154.

Kumagai, H., Palacios, P., Maeda, T., Castillo, D.B. & Nakano, M., 2009. Seismic tracking of Lahars using tremor signals, *J. Volc. Geotherm. Res.*, **183,** 112–121.

Kumagai, H., Placios, P., Ruiz, M., Yepes, H. & Kozono, T., 2011. Ascending seismic source during an explosive eruption at Tungurahua volcano, Ecuador, *Geophys. Res. Lett.*, **38,** L01306, doi:10.1029/2010GL045944.

La Rocca, M., Saccorotti, G., Del Pezzo, E. & Ibáñez, J., 2004. Probabilistic source location of explosion quakes at Stromboli volcano estimated with double array data, *J. Volc. Geotherm. Res.*, **131,** 123–142.

Lokmer, I., Bean, C.J., Saccoroti, G. & Patané, D., 2007. Moment-tensor inversion of LP events recorded on Etna in 2004 using constraints obtained from wave simulation test, *Geophys. Res. Lett.*, **34,** L22316, doi:10.1029/2007GL031902.

Lokmer, I., O'Brien, G.S., De Barros, L. & Bean, C., 2010. High resolution spatio-tempral source inversion of a long period (LP) sequence recorded by a dense broadband network, *Geophys. Res. Abstr.*, **12,** EGU2010–13706, doi:10.1029/2005GL022666.

Macedo, O., Métaxian, J.-P., Taipe, E., Ramos, D. & Inza, L.A., 2009. Seismicity associated with the 2006-2008 eruption, Ubinas volcano, *The VOLUME Project*, pp. 262–270, Bean, C.J., Braiden, A.K., Lokmer, I. Martini, F. & O'Brien, G.S., ISBN 978-1-905254-39-2.

Mars, J.I., Glangeaud, F. & L., M.J., 2004. Advanced signal processing tools for dispersive waves, *Near Surf. Geophys.*, **2**(4), 199–210.

Melnik, O. & Sparks, R.S.J., 2002. Dynamics of magma ascent and lava extrusion at Soufriere Hills volcano, Montserrat (in the eruption of Soufriere hills volcano, Montserrat from 1995 to 1999), *Mem. Geol. Soc. London*, **21,** 153–171.

Métaxian, J.-P., Lesage, P. & Valette, B., 2002. Locating sources of volcanic tremor and emergent events by seismic triangulation, *Geophys. Res. Lett.*, **107**(B10), 2243, doi:10.1029/2001JB000559.

Métaxian, J.-P., O'Brien, G., Bean, C., Valette, B. & Mora, M., 2009. Locating volcano-seismic signals in the presence of rough topography: wave simulations on Arenal volcano, Costa Rica, *Geophys. J. Int.*, **179**(3), 1547–1557.

Miron, S., Le Bihan, N. & Mars, J.I., 2005. Vector-sensor music for polarized seismic sources localization, *EURASIP J. appl. Signal Process.*, **2005,** 74–84.

Miron, S., Le Bihan, N. & Mars, J.I., 2006. High resolution vector-sensor array processing based on biquaternions, *IEEE Trans. Signal Process.*, **54,** 1218–1229.

Monteiller, V., Got, J.-L., Virieux, J. & Okubo, P., 2005. An efficient algorithm for double-difference tomography and location in heterogeneous media, with an application to the Kilauea volcano., *J. geophys. Res.*, **110,** B12306, doi:10.1029/2004JB003466.

Neuberg, J. & Pointer, T., 2000. Effects of volcano topography on seismic broad-band waveforms, *Geophys. J. Int.*, **143,** 239–248.

Neuberg, J.W., Tuffen, H., Collier, L., Green, D., Powell, T. & Dingwell, D.B., 2006. The trigger mechanism of low-frequency earthquakes on Montserrat, *J. Volc. Geotherm. Res.*, **153,** 37–50.

O'Brien, G.S. & Bean, C.J., 2004. A 3d discrete numerical elastic lattice method for seismic wave propagation in heterogeneous media with topography, *Geophys. Res. Lett.*, **31,** L14608.1–L14608.4.

O'Brien, G.S., Lokmer, I., De Barros, L., Bean, C.J., Saccoroti, G., Métaxian, J.-P. & Patané, D., 2011. Time reverse location of seismic long period events recorded on Mt Etna, *Geophys. J. Int.*, **184,** 452–462.

Ohminato, T., Chouet, B., Dawson, P. & Kedar, S., 1998. Waveform inversion of very long period impulsive signals associated with magmatic injection beneath Kilauea volcano, Hawaii, *J. geophys. Res.*, **103,** 23 823–23 826.

Papale, P., 1999. Strain-induced magma fragmentation in explosive eruptions, *Nature*, **397,** 425–428.

Paulus, C. & Mars, J.I., 2010. Vector-sensor array processing for polarization parameters and DOA estimation, *EURASIP J. Adv. Signal Process*, 850265, doi:10.1155/2010/850265.

Paulus, C., Mars, J.I. & Gounon, P., 2005. Wideband spectral matrix filtering for multicomponent sensors array, *Signal Process.*, **85,** 1723–1743.

Rivera, M., Thouret, J.-C. & Gourgaud, A., 1998. Ubinas, el volcan mas activo del sur del peru desde 1550. Geologia y evaluacion de las amenazas volcanicas., *Bol. Soc. Geol. Peru*, **88,** 53–71.

Saccorotti, G. & Del Pezzo, E., 2000. A probabilistic approach to the inversion of data from a seismic array and its application to volcanic signals, *Geophys. J. Int.*, **143,** 249–261.

Saccorotti, G., Zuccarello, L., Del Pezzo, E., Ibáñez, J. & Gresta, S., 2004. Quantitative analysis of the tremor wavefield at Etna volcano, Italy, *J. Volc. Geotherm. Res.*, **136,** 223–245.

Schmidt, R.O., 1986. Multiple emitter location and signal parameter estimation, *IEEE Trans. Antennas Prop.*, **34**(3), 276–280.

Traversa, P., Lengliné, O., Macedo, O., Métaxian, J.-P., Grasso, J., Inza, L.A. & Taipe, E., 2011. Short term forecasting of explosions at Ubinas volcano Peru, *J. geophys. Res.*, in press.

Tuffen, H. & Dingwell, D., 2005. Fault textures in volcanic conduits: evidence for seismic trigger mechanisms during silicic eruptions, *Bull. Volcanol.*, **67,** 370–387.

Tuffen, H., Dingwell, D. & Pinkerton, H., 2003. Repeated fracture and healing of silicic magma generate flow banding and earthquakes? *Geology*, **31,** 1089–1092.

Wong, K.T. & Zoltowski, M.D., 2000. Self-initiating music direction finding & polarization estimation in spatio-polarizational beamspace, *IEEE Trans. Antennas Propagat.*, **48,** 671–681.